Nanoscale

RSC Publishing

PAPER

View Article Online
View Journal | View Issue

Cite this: *Nanoscale*, 2013, **5**, 12607

Structurally tailored graphene nanosheets as lithium ion battery anodes: an insight to yield exceptionally high lithium storage performance†

Xifei Li, Yuhai Hu, Jian Liu, Andrew Lushington, Ruying Li and Xueliang Sun*

Received 10th September 2013
Accepted 6th October 2013

DOI: 10.1039/c3nr04823c

www.rsc.org/nanoscale

How to tune graphene nanosheets (GNSs) with various morphologies has been a significant challenge for lithium ion batteries (LIBs). In this study, three types of GNSs with varying size, edge sites, defects and layer numbers have been successfully achieved. It was demonstrated that controlling GNS morphology and microstructure has important effects on its cyclic performance and rate capability in LIBs. Diminished GNS layer number, decreased size, increased edge sites and increased defects in the GNS anode can be highly beneficial to lithium storage and result in increased electrochemical performance. Interestingly, GNSs treated with a hydrothermal approach delivered a high reversible discharge capacity of 1348 mA h g^{-1}. This study demonstrates that the controlled design of high performance GNS anodes is an important concept in LIB applications.

Introduction

Higher energy density and power demands required in hybrid electric vehicles (HEVs) and plug-in hybrid electric vehicles (PHEVs) have resulted in extensive research being undertaken on high theoretical capacity anodes, such as Si (4200 mA h g^{-1}) and Sn (994 mA h g^{-1}) for use in lithium ion batteries (LIBs). However, during lithium alloying/de-alloying, Si and Sn based anodes undergo enormous volume expansion in comparison to graphite,[1,2] leading to rapid capacity loss and reduced cycle life, thereby inhibiting their potential for commercialization in LIBs. Due to the disadvantages of these anodes, various allotropes of carbon, such as carbon nanotubes (CNTs), have been under intensive investigation.[3–6] Carbon-based anodes are particularly interesting due to their ability to provide fast lithium intercalation/de-intercalation activity while maintaining structural stability during charge–discharge cycles. Furthermore, their low cost and scalability makes them an attractive candidate in the practical application of LIBs.[3,4]

Graphene nanosheets (GNSs) are a recent addition to the carbon allotrope family and are comprised of a single layer of carbon atoms arranged in a hexagonal lattice connected by sp^2-hybridized bonds. The discovery of these two-dimensional carbon structures in 2004 (ref. 7) has resulted in a tremendous amount of research from the fundamental scientific community as well as from the applied research one. Vigorous research efforts have been devoted to this material due to its extraordinary and unique properties including ultra-high surface area (2630 m^2 g^{-1}), enhanced electrical conductivity (resistivity: 10^{-6} Ω cm) and superior chemical stability.[8,9] Given the aforementioned advantages and lower manufacturing costs compared to Sn- and Si-based anodes, GNSs are regarded as viable candidates for use as anode materials in LIBs. As reported, GNSs used as LIB anodes demonstrated higher reversible capacity compared to commercialized graphite.[10–22] On the other hand, graphene based nanocomposites also showed increased battery performance.[23–26] Recently, research efforts have been primarily focused on enhancing the reversible capacity of GNS anodes by various treatments,[10,12–16] including, controlling inter-graphene sheet distance,[10] as well as heteroatom doping.[16] Previous studies on other carbon allotropes have revealed that key structural parameters such as size, the number of layers, edge surface chemistry, and defect sites have a significant effect on lithium storage capacity.[27–30] Furthermore, smaller particle sized carbon anodes have been shown to deliver high specific capacities compared to their larger counterparts.[30] Density of state calculations conducted on GNSs have suggested that decreasing the graphene sheet diameter leads to a dramatic increase in lithium storage capacity.[27] Another study recently published revealed that lithium intercalation between graphene layers, in the phenolic resin derived carbon anode, results in a large number of lithium ions being doped around graphene layer edges.[29] The aforementioned findings highly suggest that structural modifications conducted on GNSs may lead to increased lithium storage capacity. Therefore, it is imperative to

Nanomaterials and Energy Lab, Department of Mechanical and Materials Engineering, University of Western Ontario, London, Ontario, N6A 5B9, Canada. E-mail: xsun@eng.uwo.ca

† Electronic supplementary information (ESI) available: SEM morphologies of GNS-I–III at low magnification, the TEM image of GNSs hydrothermally treated with urea in a ratio of 1 : 0, XPS survey, and SEM morphology changes of the three GNS anodes at low magnification after 100 charge–discharge cycles. See DOI: 10.1039/c3nr04823c

further investigate which specific structural modifications have the greatest impact on the GNS anode. This information would lead to an improved fundamental understanding concerning the facilitation of lithium ion storage in GNSs as well as providing greater insight into obtaining optimized parameters for increasing the reversible capacity of lithium ions within GNSs. Unfortunately, little attention has been paid to these interests.

Considerable efforts have been undertaken to manipulate the GNS size[31–34] including sonochemistry,[32] controlled etching,[31] particle-assisted nanocutting,[33] and controlled centrifugation.[34] However, the mass of GNSs obtained using the above methods is often too limited for use in studying LIB performance. A large number of challenges exist in attempting to modify the GNS structure while keeping the process scalable for LIB performance testing. In this regard, we have successfully developed a simple and effective approach to tune the GNS size, edge/defect sites, as well as the layer number. Three structurally modified GNSs were targeted to reveal the effect of these structural parameters on lithium storage capacity. Experiments conducted in this paper demonstrate that carefully controlled GNS production can yield tunable structural parameters such as size and layer number, which results in a significant improvement of the electrochemical performance of GNSs in LIBs. The obtained ultrathin GNS anode with decreased size and greater edge defects delivered superior discharge capacity up to 1233 mA h g^{-1}, a value higher than has been previously reported for the GNS anode. To the best of our knowledge, this is the first report to study the relationship between GNS size, edge/defect sites, the layer number and its electrochemical battery performance in LIBs. It is expected that the work presented in this paper may provide significant contributions to the development of GNS anodes for use in LIBs.

Results and discussion

Three types of GNSs (marked by GNS-I, GNS-II, and GNS-III) with altered structural morphologies were successfully synthesized using different approaches. Fig. 1 shows the morphologies and structures of GNS-I and GNS-II prepared by a modified Hummers method. These GNSs displayed flexible thin translucent nanosheets with wrinkled and curved gossamer-like structures (insets of Fig. 1a and b). In both cases, the loose GNSs exhibited a worm-like appearance and tended to overlap and stick together, resulting in the formation of agglomerates, shown in Fig. 1a and b. Sizes of GNS-I and GNS-II were measured to be approximately 7.6 μm and 7.3 μm, respectively. The representative TEM images of GNS-I and GNS-II in Fig. 1c and d show transparent gossamer characteristics, and a structure of crumpled and stacked nanosheets with the distinction of a few GNS layers.

As previously reported, the properties of GNSs are closely related to their morphologies, structures, and size.[35–37] For example, GNS size has been shown to have an impact on its electrical conductivity,[37] indicating that this parameter needs to be carefully monitored to ensure optimal battery performance. In this study, the hydrothermal treatment was employed to modify the microstructure of GNSs, moreover, a novel treatment agent of urea was firstly proposed to tailor GNSs. During the hydrothermal process, treatment time as well as the mass ratio between GNSs and urea were carefully studied. A treatment time of 3 h resulted in the process yielding an overall decrease in GNS size; however, the TEM image indicates the existence of a small number of larger sized GNSs (Fig. 2a). After a hydrothermal treatment time of 6 h, GNS particle size still decreases, however

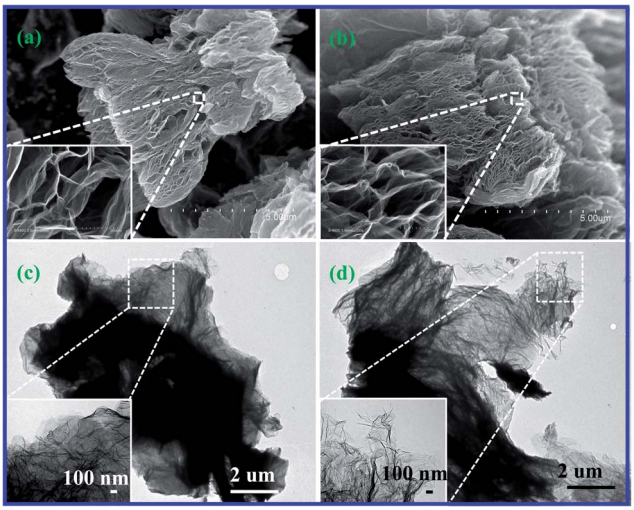

Fig. 1 Typical SEM and TEM morphologies of GNS samples: (a and c) GNS-I, (b and d) GNS-II.

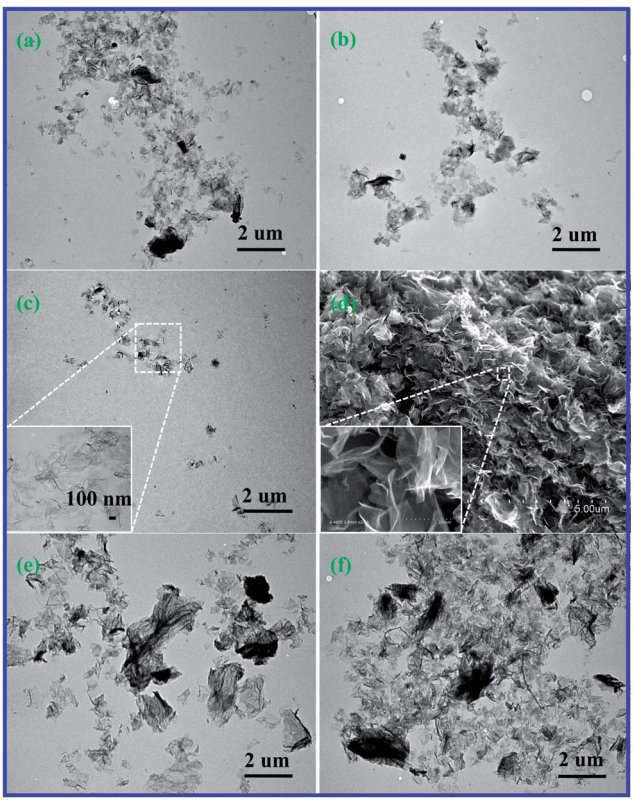

Fig. 2 TEM images of GNS-II hydrothermally treated for different times with a ratio of 1 : 300 between GNS-II and urea: (a) 3 h, (b) 6 h, and (c) 12 h; (d) SEM image of GNS-III; TEM images of GNS-II hydrothermally treated for 12 h with different ratios between GNS-II and urea: (e) 1 : 200, and (f) 1 : 100.

no larger particles were observed obviously. If treatment time was further increased to 12 h, the GNS size decreased further to a value around 400 nm. The 12 h hydrothermally treated GNSs were used in subsequent LIB studies presented in this paper and are labeled as GNS-III, shown in Fig. 2d. GNS-III displayed a different morphology compared to GNS-I and GNS-II in Fig. 1a and b. Clearly, hydrothermal treatment time has a significant effect on GNS morphology. To investigate the effect of urea on GNSs, the mass ratio of GNSs and urea was increased from 1 : 200 to 1 : 100. As shown in Fig. 2e, larger sized GNSs were obtained using a ratio of 1 : 200. When this mass ratio was increased to 1 : 100, more GNSs with larger size were observed, shown in Fig. 2f. If the mass ratio of GNSs and urea was changed to 1 : 0, *i.e.* there was no treatment agent of urea in the hydrothermal system, some GNSs were not changed at all, and retained the same size as that of GNS-II (see ESI, Fig. S2†). However, it is worth noting that the size of some GNSs decreased very much without urea for hydrothermal treatment, indicating that use of a treatment agent as well as the hydrothermal process result in a decrease of GNS size. The comparison of three types of GNSs is outlined in Scheme 1. GNS-I shows a similar size to that of GNS-II, suggesting that extended oxidation time fails to affect the GNS size. However, prolonged oxidation time results in a decrease in the number of stacked GNS layers. In contrast, 12 h hydrothermally treated GNS-III exhibits much smaller size as well as fewer layers. The obvious decrease of GNS size and the layer number is a result of the "cutting effect" that occurs during hydrothermal treatment.[38,39]

The impact of GNS size, defects and the layer number on electrochemical performance was investigated in order to determine which of the altered structural morphologies leads to enhanced lithium storage. The electrochemical properties of GNS-I–III were examined by cyclic voltammetry, at a sweep rate of 0.1 mV s^{-1} within a voltage range from 0.01 to 3.00 V (*vs.* Li/Li^+), and is shown in Fig. 3a–c. Employing a larger voltage window allows for deeper understanding of the lithium storage behavior that exists within GNSs. Three morphologically altered GNSs demonstrate similar lithium storage behaviors, indicating that size and the number of GNS layers have limited influence on lithium intercalation/de-intercalation kinetics. All three GNSs displayed a prominent peak within the first reduction of the discharge sweep, strongly suggesting the formation of a solid-electrolyte-interphase (SEI) film on GNSs. However, peak location varied between the GNSs and moved from about 0.60, 0.66, and 0.69 V for GNS-I, GNS-II, and GNS-III, respectively. Subsequent discharge cycles lead to a loss of the SEI-derived peak due to the formation of a dense SEI film around the anode resulting in a greater separation between the GNS and electrolyte.[6,16] Furthermore, the peak located close to 0 V within the CV curves of GNS-I–III can be attributed to lithium intercalation into GNSs.

Voltage profiles of GNS anodes in a voltage window of 0.01–3.00 V within the 1st, 2nd, 50th, and 100th cycle at a current density of 100 mA g^{-1} are shown in Fig. 3d–f. All three structurally altered GNSs exhibited similar charge–discharge profiles in their high voltage hysteresis. Interestingly, no obvious potential plateaus were observed in the charge–discharge processes of GNS-I–III anodes, as previously reported.[12,16,40] The absence of this plateau indicates the existence of electrochemically and geometrically nonequivalent lithium storage sites within the GNS anodes.[15,16] The discharge (lithium-intercalation) of GNS-I and GNS-II occurred at 925 and 418 mA h g^{-1} while the charge (lithium-de-intercalation) capacities of GNS-I and GNS-II occurred at 1275 and 861 mA h g^{-1} within the first cycle. During the second discharge process, GNS-I and GNS-II demonstrated a reversible capacity of 407 and 723 mA h g^{-1}, respectively. However, GNS-III delivered a very high specific capacity in the first cycle (charge capacity of 1233 mA h g^{-1} and discharge capacity of 2561 mA h g^{-1}), while its reversible discharge capacity during the 2nd cycle reached a value of 1348 mA h g^{-1}. For these three GNS anodes, the irreversible capacity loss in the first cycle might be attributed to SEI formation. Evidently, as illustrated in Fig. 3d–f, these three GNSs exhibited charge–discharge curves typically seen in previous studies.[16,17,41] Fig. 3d–f also indicate that the three anodes showed similar lithium storage behaviors from the 1st cycle to the 100th cycle.

The cyclic performance of GNS-I–III was compared, as shown in Fig. 4a. GNS-I displayed the worst cycling performance with a

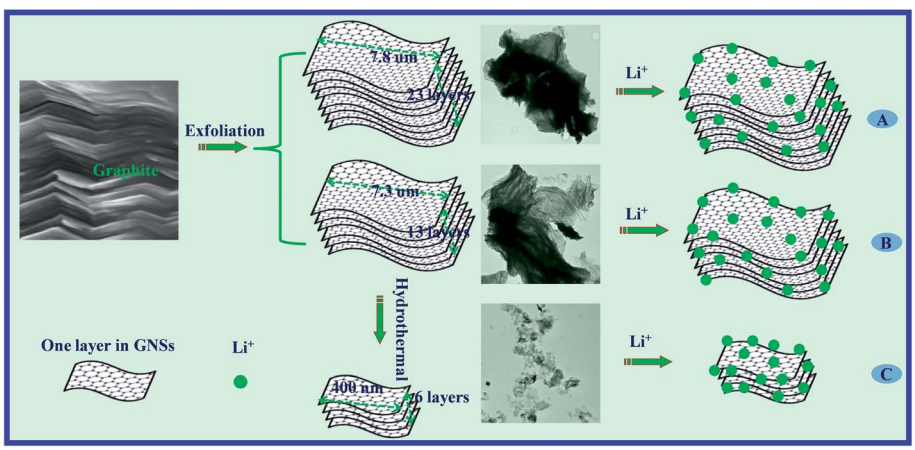

Scheme 1 Schematic illustration of morphological evolution and lithium storage of three types of GNSs: (A) GNS-I; (B) GNS-II; and (C) GNS-III.

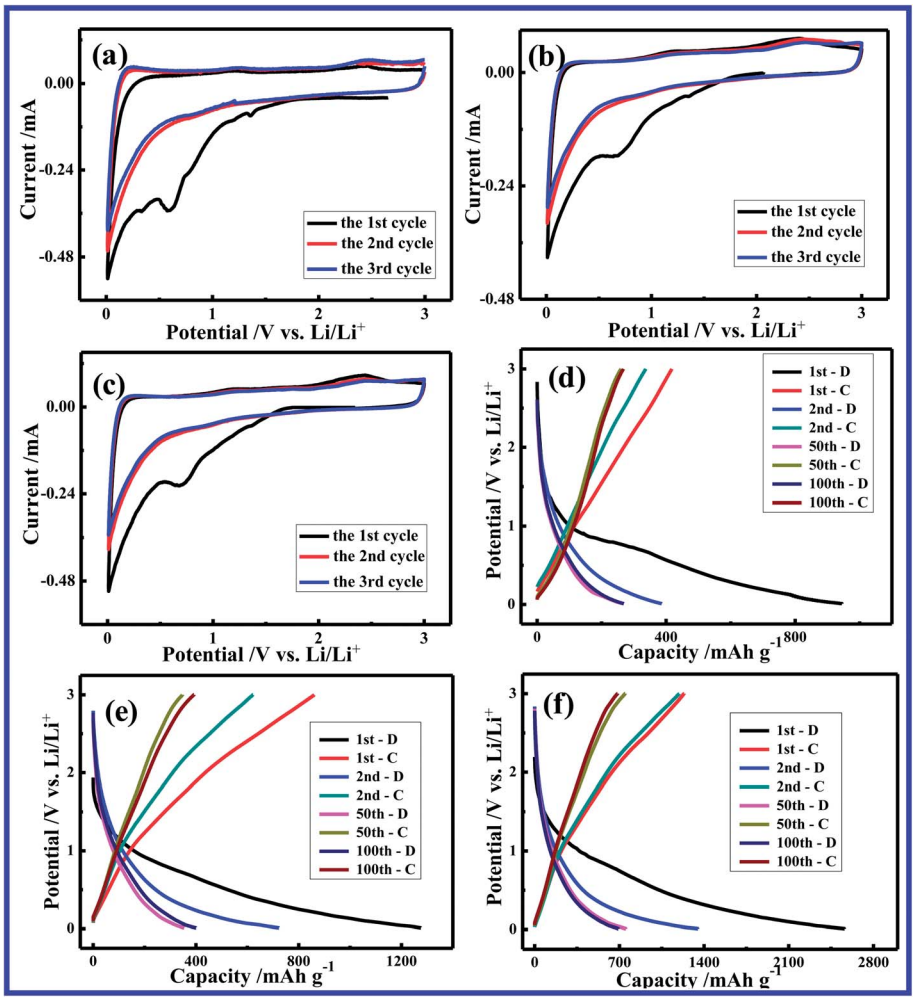

Fig. 3 Cyclic voltammograms and charge–discharge profiles of three types of GNSs: (a and d) GNS-I, (b and e) GNS-II, and (c and f) GNS-III.

discharge capacity of 269 mA h g^{-1} in the 100th cycle, a value lower than the conventional graphite anode. By contrast, GNS-II revealed enhanced battery performance and delivered a high discharge capacity of 400 mA h g^{-1} after 100 cycles. Among the three structurally modified anodes, GNS-III demonstrated the best cycling performance while maintaining a high energy capacity of 691 mA h g^{-1} in the 100th discharge cycle. Furthermore, varying levels of coulombic efficiency were observed for the three GNS anodes, as outlined in Fig. 4b. GNS-III displayed almost 100% coulombic efficiency and maintained longer stability compared to the GNS produced by conventional thermal exfoliation.

Rate capability is a crucial performance factor for application of LIBs in HEVs/PHEVs, which require relatively rapid discharge–charge rates.[42,43] The remarkable cycling performance exhibited by GNSs motivated further investigation into the rate capability using varying current rates, as shown in Fig. 4c. GNS-III anodes displayed elevated capacity and superior stability at each current density, compared to GNS-II, regardless of current density. For both anodes, an increase in charge–discharge current density resulted in decreased discharge capacity. This result is attributed to a low lithium diffusion rate as well as an over-potential at the anodes, resulting from limited lithium diffusion kinetics.[6,44,45] Fig. 4d displays the discharge capacities of the second cycle at various current densities and are compared with the capacity at 100 mA g^{-1}. GNS-III demonstrated higher capacity retention percent at 200, 400, 800 and 1200 mA g^{-1} than the GNS-II anode, indicating that GNS-III possesses superior rate capability in LIB performance.

Based on the results mentioned above, three morphologically altered GNS anodes revealed varying electrochemical performance. In this study, hydrothermally treated GNSs dramatically increased the reversible capacity, cycling performance and rate capability compared to thermally exfoliated GNSs. It is evident that structural parameters such as surface functional groups, surface defects, heteroatom doping, layers, size and edges of GNSs have a significant impact on battery performance. In order to gain a better understanding of the impact of key structural parameters on the improvement of lithium storage performance, the aforementioned five structural considerations of the GNS anode are discussed as below.

(1) Surface functional groups of GNS-I–III were characterized by FTIR spectra, as shown in Fig. 5a. The obtained FTIR spectra of the GNSs displayed the following similar peaks: (a) a strong

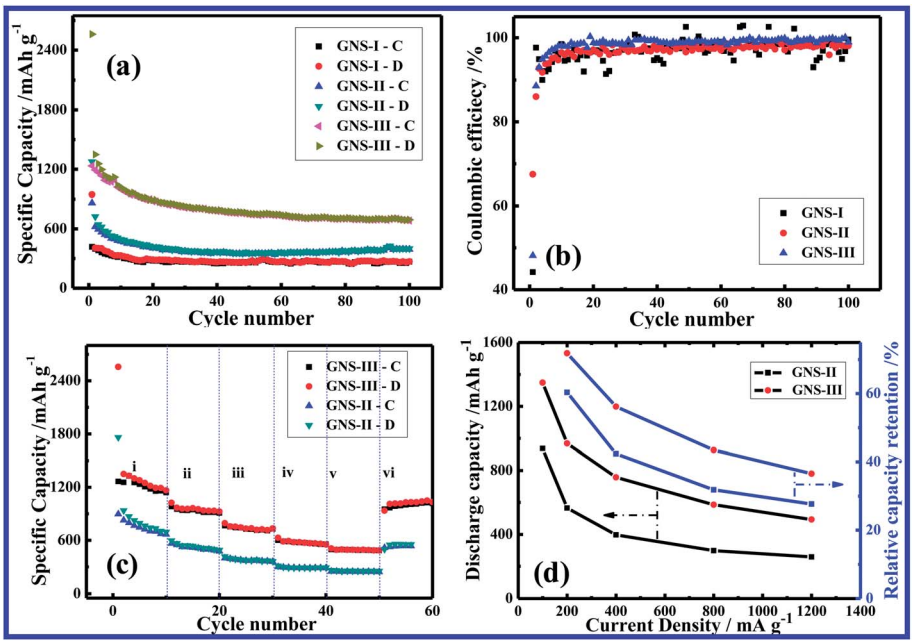

Fig. 4 (a) Reversible charge–discharge capacity against cycle numbers of various GNSs at a current density of 100 mA g^{-1} in a voltage window of 0.01–3.00 V; (b) Coulombic efficiency against cycle numbers of various GNSs; (c) rate capability of GNS-II and GNS-III at various current densities: (i) 100, (ii) 200, (iii) 400, (iv) 800, (v) 1200, and (vi) 100 mA g^{-1}; (d) at the second cycle the discharge capacities of GNS-II and GNS-III as a function of current density from 100 mA g^{-1} to 1200 mA g^{-1} and relative capacity retention at 200, 400, 800, and 1200 mA g^{-1} in comparison to the discharge capacity at 100 mA g^{-1}.

and broad hydroxyl peak around 3456 cm^{-1}; (b) peaks positioned at 1635, 1390, 1255, and 1073 cm^{-1} resulting from C=C in carboxyl, un-oxidized graphitic domains/adsorbed water molecules, O–H, C–OH, and C–O groups; and (c) two small peaks at 802 and 667 cm^{-1} corresponding to the existence of epoxide or peroxide groups on the surface.[35] These results indicate that similar oxygen functional groups exist on all three GNSs, suggesting that size, edge sites, GNS layers, as well as treatment processes, have limited impact on the presence of surface functional groups.

(2) Fig. 5b displays Raman spectra obtained for GNS-I–III. Two characteristic bands exist in the Raman spectra, the G band with E_{2g} symmetry, ascribed to ordered sp^2 carbon at ~1590 cm^{-1} and a D band with A_{1g} symmetry at ~1353 cm^{-1}, ascribed to disordered carbon, edge defects, and other defects oriented sp^3 bonded carbons such as, dangling bonds, vacancies, and topological defects. Both bands originate from a Raman active in-plane tangential stretching mode that exists in carbon–carbon bonds within highly oriented pyrolytic graphite as well as disorder induced features resulting from finite particle size and/or lattice distortion effects.[46,47] I_D and I_G correspond to the intensity of the scattering disordered and ordered sp^2 bonding carbon atoms, respectively. The ratio of I_D/I_G is typically used as a gauge in determining the graphitic degree of carbon.[42,48] Calculated I_D/I_G ratios for GNS-I, GNS-II, and GNS-III were 0.66, 0.67 and 0.88, respectively. Interestingly, the elevated I_D/I_G value for GNS-III compared to GNS I and II indicates that the hydrothermal treatment process of reducing GNS size also results in an increase in defect sites.

(3) Urea, used as a treatment agent during the hydrothermal process of GNS-III, contains elemental nitrogen. As a result, urea holds the possibility of providing heteroatom nitrogen doping of GNSs during hydrothermal treatment.[49–51] XPS characterization performed on GNS-III, shown in Fig. S3,† indicates the existence of C1s and O1s peaks located at 285 eV and 531 eV, respectively. The lack of XPS data towards elemental nitrogen indicates that doping did not occur during hydrothermal treatment of GNS with urea.

(4) The GNS layer number of all three samples was estimated using cross-sectional HRTEM images, shown in Fig. 5c–e. The images revealed that GNS I–III exhibited varying numbers of graphene layers. GNS-I was found to possess ~23 graphene stacking layers while an increase of oxidation time resulted in a decreased layer number with GNS-II containing only ~13 layers. Interestingly, GNS-III treated by the hydrothermal process demonstrated a further reduction in the layer number and contained ~6 GNS layers.

(5) SEM and TEM images, shown in Fig. 1 and 2, clearly indicate the presence of a size distinction among produced GNSs. It is evident that the "cutting effect" of the hydrothermal treatment on GNS-III results in a dramatic decrease in particle size, down to ~400 nm. Comparatively, GNS-I and GNS-II indicated the average particle size to be 7–8 μm. Furthermore, the decrease in GNS-III size results in a higher concentration of edge sites at the periphery of the nanodomains, compared to larger sized GNS-I and GNS-II particles.[12,52] This may also be the result of an increased I_D/I_G ratio seen during Raman spectroscopy.

Based on the above analysis, GNS-III is smaller in size with fewer layers and contains a greater number of defects compared to GNS-I and GNS-II. Therefore, the enhanced reversible capacity observed in GNS-III may be attributed to these structural modifications. A lithium storage model of GNS-I, GNS-II,

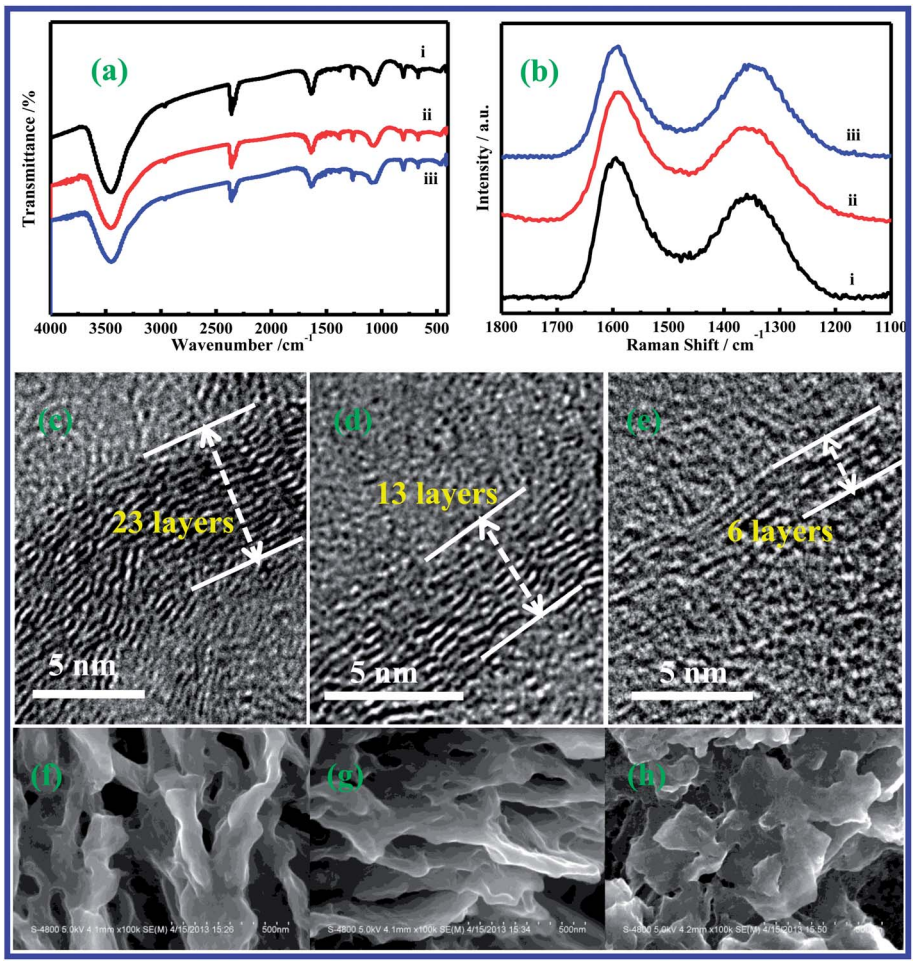

Fig. 5 (a) FT-IR and (b) Raman spectra of three GNS samples: (i) GNS-I, (ii) GNS-II, and (iii) GNS-III; cross-sectional HRTEM images of three types of GNSs: (c) GNS-I, (d) GNS-II, and (e) GNS-III; morphologies of these three GNS anodes after 100 charge–discharge cycles at a current density of 100 mA g^{-1} in a voltage window of 0.01–3.00 V: (f) GNS-I, (g) GNS-II, and (h) GNS-III.

and GNS-III is outlined in Scheme 1. (i) As reported, a decrease of GNS size results in an increase of available graphene edge sites, and may determine important properties of GNSs.[53,54] Previous reports have indicated that the carbon atoms at the edge of graphene displayed elevated activity and energy compared to sp^2 bonded carbon atoms located within the basal plane.[55] As a result, the smaller sized GNS-III anode with pronounced edge sites possesses the capability of encouraging increased lithium storage. (ii) The higher I_D/I_G value of GNS-III given by Raman spectroscopy indicates the presence of increased disorder, a larger number of defects, and decreased sp^2 domains. These parameters encourage additional lithium storage sites on the GNS anode, and thereby result in an increased energy capacity.[12,16,30,56] (iii) Previous studies have indicated that lithium can be effectively adsorbed on both sides of GNSs that arrange like a "house of cards" in hard carbon anodes, doubling the amount of stored lithium for individual graphene sheets, thus proving that the number of GNS layers has a significant effect on lithium storage capability.[27,46,57] (iv) An increase of nanocavities and nanovoids present in the GNSs resulting from scrolling and crumpling of nanosheets can have a significant contribution to the specific capacity of the anodes.[58,59] Therefore, GNS-III with smaller size, more edge sites, greater defects, and fewer layers may result in enhanced lithium storage and have tremendous advantage in the application for LIBs. However, the electrical conductivity of the GNS anode will be greatly decreased if the GNS size is decreased down to several nanometers. The derived results may be different that the anode performance improvement will be suppressed because of the low electrical conductivity.

Unfortunately, the capacity fade seen in the first 20 cycles shown in Fig. 4a is a phenomenon commonly demonstrated within GNS anodes used in LIBs, and serves as a hindering factor in their application as LIB anodes.[10,13,16,46,59] Morphological changes in GNS anodes after 100 charge–discharge cycles are presented in Fig. 5f–h (low magnification morphologies presented in Fig. S4†). After repeated lithium intercalation/de-intercalation, a thin translucent film can be seen in all GNS anodes, originating from SEI formation. The thin film results in irreversible capacity loss of GNS anodes as lithium diffusion is hindered by this film. However, GNS-III retains its characteristic nanosheets better under electrochemical reaction with lithium compared to GNS-I and GNS-II, and provides the possibility of better cyclic performance as an anode material for LIBs.

Conclusions

In summary, the controlled synthesis of three types of GNSs with varying size, edge sites, defects and layer numbers has been successfully achieved. The effect of these morphological changes on the electrochemical performance of GNSs as anode materials in LIBs has been investigated. This study demonstrates the significant importance of controlling the GNS morphology and microstructure in improving its cyclic performance and rate capability in LIBs. Diminished GNS layer number, decreased size, increased edge sites and increased defects in the GNS anode can be highly beneficial to lithium storage and result in increased electrochemical performance. GNS-III, produced by hydrothermal treatment, reached a high reversible discharge capacity of 1348 mA h g^{-1}, and demonstrated an elevated value of 691 mA h g^{-1} in the 100th cycle. Comparatively, GNS-I and II revealed a much lower reversible capacity after 100 cycles with a value of 269 and 400 mA h g^{-1}, respectively. The fabrication of a superior GNS-III anode can be achieved *via* a simple, quick, and inexpensive approach. This paper demonstrates that the controlled design of high performance GNS anodes is an important concept and indicates that precise manipulation of the GNS structure may serve as a crucial stepping stone towards the future commercialization of graphene-based electrodes in LIB applications.

Experimental section

Synthesis of GNS-I

Graphene oxide was first prepared by the modified Hummers method.[60] Graphite powder (1 g, flakes (Aldrich)) was mixed with concentrated H_2SO_4 (23 mL) and stirred at room temperature for 0.5 h. $NaNO_3$ (0.5 g) was added into the mixture and left overnight. Then, the reaction vessel was immersed in an ice water bath, and $KMnO_4$ (3 g) was added slowly and stirred for 2 h. After the dilution with DI water (46 mL), 30% H_2O_2 was added to the mixture, and the color of the mixture changed into a brilliant yellow along with violent bubbling. Finally, the mixture was filtered and washed with HCl aqueous solution to remove residual metal ions, then washed with DI water until pH = 7. The slurry was dried in air. The resulting solid (graphene oxide) was inserted into a quartz tube in an argon atmosphere. The quartz tube was quickly inserted into a preheated furnace at 1050 °C for 30 s. This treatment was used to promote the exfoliation of the graphene sheets and reduce the oxygen moieties.

Synthesis of GNS-II

After $KMnO_4$ (3 g) was added, the stirring time was changed from 2 h to 120 h. Other steps were the same as those for the synthesis of GNS-I.

Synthesis of GNS-III

A hydrothermal process was performed to modify GNS-II to obtain GNS-III as below. GNS-II (20 mg) was dispersed into deionized water (35 mL) under sonication for 1 h, and then various amounts of urea (the mass ratio between GNS-II and urea is 1 : 0, 1 : 100, 1 : 200, and 1 : 300) were added. The resulting suspension was sealed in a Teflon-lined autoclave and maintained at 180 °C for different times (3, 6, and 12 h). The solids were filtered and washed with distilled water several times, and then were dried in a vacuum oven at 90 °C overnight. GNSs obtained by hydrothermal treatment for 12 h with urea in a ratio of 1 : 300 was marked GNS-III.

Characterization of as-synthesized GNSs

The morphologies of GNSs were examined using a field emission scanning electron microscope (FE-SEM, Hitachi S-4800), a transmission electron microscope (TEM, Hitachi H-7000), and a high-resolution transmission electron microscope (HRTEM, JEOL 2010F). Powder X-ray diffraction (XRD) patterns were recorded using a Rigaku RU-200BVH diffractometer employing a Co-K_α source (λ = 1.7892 Å). Raman spectra were obtained using a HORIBA Scientific LabRAM HR Raman spectrometer system equipped with a 532.4 nm laser as the exciting radiation equipped with an optical microscope at room temperature. Fourier transform-infrared (FT-IR) spectroscopy was performed using a Nicolet 6700 FT-IR spectrometer. FT-IR spectra were obtained in the transmittance mode in a range of 400–4000 cm^{-1}.

Electrochemical storage behavior of GNSs

A 2032 coin-type electrochemical half-cell included a working electrode, a lithium foil as the counter electrode, and a Celgard 2400 separator. Working electrodes were prepared by slurry casting on a Cu foil as a current collector. The slurry contained GNSs (90 wt% on dry solids basis) and a polyvinylidene fluoride binder (10 wt% on dry solids basis) in *N*-methylpyrrolidinone (NMP) solvent. The electrodes were dried in a vacuum at 90 °C overnight. The electrolyte was composed of 1 M $LiPF_6$ salt dissolved in ethylene carbonate (EC)–diethyl carbonate (DEC)–ethyl methyl carbonate (EMC) in a 1 : 1 : 1 volume ratio. CR-2032-type coin cells were assembled in a glove box under a dry argon atmosphere (moisture and oxygen concentration <1 ppm). Cyclic voltammetry tests were performed on a versatile multichannel potentiostat 3/Z (VMP3) at a scan rate of 0.1 mV s^{-1} over a potential range of 0.01 to 3.0 V (*vs.* Li/Li^+). Charge–discharge characteristics were tested galvanostatically between 0.01 and 3.0 V (*vs.* Li/Li^+) at room temperature using an Arbin BT-2000 Battery Tester.

Acknowledgements

This research was supported by the Natural Science and Engineering Research Council of Canada (NSERC), General Motors, Canada Research Chair (CRC) Program, Canadian Foundation for Innovation (CFI), Ontario Research Fund (ORF), Early Researcher Award (ERA) and the University of Western Ontario. X. Li is grateful to Springpower International, Inc. and the MITACS Elevate Strategic Fellowship Program.

Notes and references

1 C. K. Chan, H. Peng, G. Liu, K. McIlwrath, X. F. Zhang, R. A. Huggins and Y. Cui, *Nat. Nano*, 2008, **3**, 31–35.
2 Y. Liu, J. Y. Xie and J. Yang, *J. Power Sources*, 2003, **119–121**, 572–575.
3 J. R. Dahn, T. Zheng, Y. Liu and J. S. Xue, *Science*, 1995, **270**, 590–593.
4 N. Takami, A. Satoh, M. Hara and T. Ohsaki, *J. Electrochem. Soc.*, 1995, **142**, 371–379.
5 M. Yoshio, H. Wang, K. Fukuda, Y. Hara and Y. Adachi, *J. Electrochem. Soc.*, 2000, **147**, 1245–1250.
6 X. Li, J. Liu, Y. Zhang, Y. Li, H. Liu, X. Meng, J. Yang, D. Geng, D. Wang, R. Li and X. Sun, *J. Power Sources*, 2012, **197**, 238–245.
7 K. S. Novoselov, A. K. Geim, S. V. Morozov, D. Jiang, Y. Zhang, S. V. Dubonos, I. V. Grigorieva and A. A. Firsov, *Science*, 2004, **306**, 666–669.
8 M. J. Allen, V. C. Tung and R. B. Kaner, *Chem. Rev.*, 2009, **110**, 132–145.
9 M. D. Stoller, S. Park, Y. Zhu, J. An and R. S. Ruoff, *Nano Lett.*, 2008, **8**, 3498–3502.
10 E. Yoo, J. Kim, E. Hosono, H.-s. Zhou, T. Kudo and I. Honma, *Nano Lett.*, 2008, **8**, 2277–2282.
11 A. V. Murugan, T. Muraliganth and A. Manthiram, *Chem. Mater.*, 2009, **21**, 5004–5006.
12 D. Pan, S. Wang, B. Zhao, M. Wu, H. Zhang, Y. Wang and Z. Jiao, *Chem. Mater.*, 2009, **21**, 3136–3142.
13 P. Lian, X. Zhu, S. Liang, Z. Li, W. Yang and H. Wang, *Electrochim. Acta*, 2010, **55**, 3909–3914.
14 T. Bhardwaj, A. Antic, B. Pavan, V. Barone and B. D. Fahlman, *J. Am. Chem. Soc.*, 2010, **132**, 12556–12558.
15 S.-H. Lee, S.-D. Seo, Y.-H. Jin, H.-W. Shim and D.-W. Kim, *Electrochem. Commun.*, 2010, **12**, 1419–1422.
16 X. Li, D. Geng, Y. Zhang, X. Meng, R. Li and X. Sun, *Electrochem. Commun.*, 2011, **13**, 822–825.
17 R. Mukherjee, A. V. Thomas, A. Krishnamurthy and N. Koratkar, *ACS Nano*, 2012, **6**, 7867–7878.
18 A. L. M. Reddy, A. Srivastava, S. R. Gowda, H. Gullapalli, M. Dubey and P. M. Ajayan, *ACS Nano*, 2010, **4**, 6337–6342.
19 S.-H. Lee, V. Sridhar, J.-H. Jung, K. Karthikeyan, Y.-S. Lee, R. Mukherjee, N. Koratkar and I.-K. Oh, *ACS Nano*, 2013, **7**, 4242–4251.
20 A. Kumar, A. L. M. Reddy, A. Mukherjee, M. Dubey, X. Zhan, N. Singh, L. Ci, W. E. Billups, J. Nagurny, G. Mital and P. M. Ajayan, *ACS Nano*, 2011, **5**, 4345–4349.
21 Z.-S. Wu, W. Ren, L. Xu, F. Li and H.-M. Cheng, *ACS Nano*, 2011, **5**, 5463–5471.
22 Z.-l. Wang, D. Xu, Y. Huang, Z. Wu, L.-m. Wang and X.-b. Zhang, *Chem. Commun.*, 2012, **48**, 976–978.
23 X.-l. Huang, R.-z. Wang, D. Xu, Z.-l. Wang, H.-g. Wang, J.-j. Xu, Z. Wu, Q.-c. Liu, Y. Zhang and X.-b. Zhang, *Adv. Funct. Mater.*, 2013, **23**, 4345–4353.
24 Y. Huang, X.-l. Huang, J.-s. Lian, D. Xu, L.-m. Wang and X.-b. Zhang, *J. Mater. Chem.*, 2012, **22**, 2844–2847.
25 H. Wang, D. Ma, X. Huang, Y. Huang and X. Zhang, *Sci. Rep.*, 2012, **2**, 701.
26 X. Li, X. Meng, J. Liu, D. Geng, Y. Zhang, M. N. Banis, Y. Li, J. Yang, R. Li, X. Sun, M. Cai and M. W. Verbrugge, *Adv. Funct. Mater.*, 2012, **22**, 1647–1654.
27 A. Gerouki, M. A. Goldner, R. B. Goldner, T. E. Haas, T. Y. Liu and S. Slaven, *J. Electrochem. Soc.*, 1996, **143**, L262–L263.
28 Y. Matsumura, S. Wang and J. Mondori, *Carbon*, 1995, **33**, 1457–1462.
29 H. Q. Xiang, S. B. Fang and Y. Y. Jiang, *J. Electrochem. Soc.*, 1997, **144**, L187–L190.
30 M. Winter, J. O. Besenhard, M. E. Spahr and P. Novák, *Adv. Mater.*, 1998, **10**, 725–763.
31 D. Wei and Y. Liu, *Adv. Mater.*, 2010, **22**, 3225–3241.
32 Z.-S. Wu, W. Ren, L. Gao, B. Liu, J. Zhao and H.-M. Cheng, *Nano Res.*, 2010, **3**, 16–22.
33 L. Ci, Z. Xu, L. Wang, W. Gao, F. Ding, K. Kelly, B. Yakobson and P. Ajayan, *Nano Res.*, 2008, **1**, 116–122.
34 U. Khan, A. O'Neill, H. Porwal, P. May, K. Nawaz and J. N. Coleman, *Carbon*, 2012, **50**, 470–475.
35 C. Ma, Z. Chen, M. Fang and H. Lu, *J. Nanopart. Res.*, 2012, **14**, 1–9.
36 L. Ćirić, A. Sienkiewicz, D. M. Djokić, R. Smajda, A. Magrez, T. Kaspar, R. Nesper and L. Forró, *Phys. Status Solidi B*, 2010, **247**, 2958–2961.
37 L. Zhang, J. Liang, Y. Huang, Y. Ma, Y. Wang and Y. Chen, *Carbon*, 2009, **47**, 3365–3368.
38 D. Pan, J. Zhang, Z. Li and M. Wu, *Adv. Mater.*, 2010, **22**, 734–738.
39 S. Kim, S. W. Hwang, M.-K. Kim, D. Y. Shin, D. H. Shin, C. O. Kim, S. B. Yang, J. H. Park, E. Hwang, S.-H. Choi, G. Ko, S. Sim, C. Sone, H. J. Choi, S. Bae and B. H. Hong, *ACS Nano*, 2012, **6**, 8203–8208.
40 Z.-L. Wang, D. Xu, H.-G. Wang, Z. Wu and X.-B. Zhang, *ACS Nano*, 2013, **7**, 2422–2430.
41 Z.-S. Wu, L. Xue, W. Ren, F. Li, L. Wen and H.-M. Cheng, *Adv. Funct. Mater.*, 2012, **22**, 3290–3297.
42 X. Li, A. Dhanabalan, L. Gu and C. Wang, *Adv. Energy Mater.*, 2012, **2**, 238–244.
43 D. Liu and G. Cao, *Energy Environ. Sci.*, 2010, **3**, 1218–1237.
44 X. F. Li, A. Dhanabalan, K. Bechtold and C. L. Wang, *Electrochem. Commun.*, 2010, **12**, 1222–1225.
45 H. Buqa, D. Goers, M. Holzapfel, M. E. Spahr and P. Novák, *J. Electrochem. Soc.*, 2005, **152**, A474–A481.
46 G. Wang, X. Shen, J. Yao and J. Park, *Carbon*, 2009, **47**, 2049–2053.
47 J. Shen, Y. Hu, C. Qin and M. Ye, *Langmuir*, 2008, **24**, 3993–3997.
48 X. Li, J. Yang, Y. Hu, J. Wang, Y. Li, M. Cai, R. Li and X. Sun, *J. Mater. Chem.*, 2012, **22**, 18847–18853.
49 Z. Wang, R. Jia, J. Zheng, J. Zhao, L. Li, J. Song and Z. Zhu, *ACS Nano*, 2011, **5**, 1677–1684.
50 X. Y. Chen, C. Chen, Z. J. Zhang, D. H. Xie, X. Deng and J. W. Liu, *J. Power Sources*, 2013, **230**, 50–58.
51 B. Zheng, J. Wang, F.-B. Wang and X.-H. Xia, *Electrochem. Commun.*, 2013, **28**, 24–26.

52 V. Mussi, P. Fanzio, G. Firpo, L. Repetto and U. Valbusa, *Nanotechnology*, 2012, **23**, 435301.
53 K. A. Ritter and J. W. Lyding, *Nat. Mater.*, 2009, **8**, 235–242.
54 D. Deng, L. Yu, X. Pan, S. Wang, X. Chen, P. Hu, L. Sun and X. Bao, *Chem. Commun.*, 2011, **47**, 10016–10018.
55 X. Wang and H. Dai, *Nat. Chem.*, 2010, **2**, 661–665.
56 Y. Shen, H.-B. Zhang, H. Zhang, W. Ren, A. Dasari, G.-S. Tang and Z.-Z. Yu, *Carbon*, 2013, **56**, 132–138.
57 X. Tong, H. Wang, G. Wang, L. Wan, Z. Ren, J. Bai and J. Bai, *J. Solid State Chem.*, 2011, **184**, 982–989.
58 H. Kim, Z. Wen, K. Yu, O. Mao and J. Chen, *J. Mater. Chem.*, 2012, **22**, 15514–15518.
59 P. Guo, H. Song and X. Chen, *Electrochem. Commun.*, 2009, **11**, 1320–1324.
60 W. S. Hummers and R. E. Offeman, *J. Am. Chem. Soc.*, 1958, **80**, 1339.